



Supplement of

Spectral attenuation coefficients from measurements of light transmission in bare ice on the Greenland Ice Sheet

Matthew G. Cooper et al.

Correspondence to: Matthew G. Cooper (guycooper@ucla.edu)

The copyright of individual parts of the supplement might differ from the article licence.

1 **S1 Monte Carlo radiative transfer model**

2 The Monte Carlo method solves the radiative transfer equation (RTE) by simulating large ensembles of photon events
3 represented by random samples from probability density functions (Ertürk and Howell, 2017). In this study and others,
4 the Monte Carlo method is used to quantify relative uncertainties in imperfect optical measurements that are intractable
5 with analytical or numerical solutions to the RTE (Gordon, 1985). The model we developed to estimate the effect of
6 detector interference on our irradiance measurements closely follows methods developed to simulate light propagation
7 in biological tissue, ocean waters, and sea ice (Leathers et al., 2004; Light et al., 2003; Wang et al., 1995). A general
8 description of the model and particular modifications for this investigation are described below.

9 **S1.1 Probability functions for optical properties**

10 The fundamental ingredients of this and other Monte Carlo radiative transfer models are the inherent optical properties
11 k , ω , and g (see Sect. 2.3 of the main), the geometric boundary conditions, and the probabilistic rules that govern the
12 system. The cumulative probability of occurrence for an event x , with probability density function $p(x)$, is:

$$13 \quad P(x) = \int_{-\infty}^x p(x)dx, \quad 0 \leq P(x) \leq 1. \quad (1)$$

14 To solve for x , the left-hand-side (LHS) of (1) is replaced with a random number:

$$15 \quad P(x) = q \quad (2)$$

16 where q is from the uniform distribution over $[0,1]$. The right-hand-side (RHS) lower limit of integration $-\infty$ is
17 replaced with an appropriate limit (e.g., 0) and analytic or empirical expressions for $p(x)$ are specified.

18
19 In this study, x represents optical path length, scattering direction, and photon survival probability. Closed-form
20 expressions for each of these terms are given in the following sections.

21 **S1.1.1 Optical path length**

22 The probability density function for the optical path length l [m^{-1}] is given by the e-folding length:

$$23 \quad p(l) = e^{-l}, \quad l \geq 0 \quad (3)$$

24 with the cumulative distribution function:

$$25 \quad P(l) = \int_0^l e^{-l'} dl' = 1 - e^{-l}. \quad (4)$$

26 From Eq. (2), $q = 1 - e^{-l}$ and therefore:

$$27 \quad l = -\ln q, \quad 0 \leq 1. \quad (5)$$

28 In this study, q is generated with the MATLAB® function rand.

29
30 The photon transport length [m] is the optical path length scaled by the extinction coefficient:

31
$$s = l/\sigma_e \quad (6)$$

32 where:

33
$$\sigma_e = \sigma_s + \sigma_a \quad (7)$$

34 is the single-scattering extinction coefficient, σ_s [m^{-1}] is the scattering coefficient, and σ_a [m^{-1}] is the absorption
35 coefficient.

36 S1.1.2 Scattering phase function

37 The probability density function for a scattering phase function with azimuthal symmetry is:

38
$$p(\theta_s) = 2\pi\tilde{\beta}(\theta_s) \sin \theta \quad (8)$$

39 where $\tilde{\beta}(\theta_s)$ is the probability that a photon will scatter at polar angle θ_s . We specify $\tilde{\beta}(\theta_s)$ with the
40 Henyey-Greenstein scattering phase function, which is appropriate for strongly forward scattering by ice grains and
41 air bubbles (Light et al., 2003):

42
$$\tilde{\beta}(g, \theta_s) = \frac{1}{4\pi} \frac{1 - g^2}{(1 + g^2 - 2g \cos \theta_s)^{\frac{3}{2}}}, \quad -1 < g < 1. \quad (9)$$

43 where $g = 0$ reduces Eq. 9 to isotropic scattering and $g \rightarrow 1$ is strongly forward scattering. In this study, $g = 0.86$, as
44 given by Mullen & Warren (1988) from Mie theory calculations for scattering by air bubbles in ice.

45 From Eq. (1):

47
$$P(\theta_s) = -\frac{1 - g^2}{2} \int_0^{\theta_s} \frac{\sin \theta'_s}{(1 + g^2 - 2g \cos \theta'_s)^{\frac{3}{2}}} d\theta'_s = q \quad (10)$$

48 which evaluates to:

49
$$q = \frac{1 - g^2}{2g} \left[\frac{1}{1 - g} - \frac{1}{\sqrt{1 + g^2 - 2g \cos \theta_s}} \right] \quad (11)$$

50 yielding the scattering angle:

52
$$\cos \theta_s = \frac{1}{2g} \left[1 + g^2 - \left(\frac{1 - g^2}{1 - g + 2gq} \right)^2 \right], \quad g \neq 0; 0 \leq \theta_s \leq \pi/2. \quad (12)$$

53 The probability density function for scattering azimuth angle ϕ_s in a spherical coordinate system with azimuthal
54 symmetry is $1/2\pi$. From Eq. (1):

55
$$P(\phi_s) = \frac{\phi_s}{2\pi}, \quad 0 \leq \phi_s \leq 2\pi \quad (13)$$

56 and from Eq. (2):

57
$$\phi_s = 2\pi q. \quad (14)$$

58 S1.1.3 Photon termination

59 Monte Carlo simulations are computationally expensive. To improve performance, photons are treated as packets of
 60 photons with initial weight $w = 1$. At each interaction, photons are scattered and absorbed in proportion to their
 61 respective statistical probabilities, parameterized by σ_s and σ_a . Accordingly, at each interaction the weight is updated
 62 as:

$$63 \quad w = (1 - \bar{\omega}) \cdot w \quad (15)$$

64 where:

$$65 \quad \bar{\omega} = \sigma_s / \sigma_e \quad (16)$$

66 is the single-scattering albedo [-]. Each $1 - \bar{\omega}$ reduction in photon packet weight is proportional to the probability of
 67 an individual photon absorption event. After many interactions, if w drops below a very small value it contributes
 68 very little to the solution. The so-called “Russian roulette” technique is used to improve computational performance,
 69 where photon packet weights below a specified threshold $w < w_{\min}$ are increased in proportion to a survival
 70 probability function and are re-released into the medium, or otherwise terminated:

$$71 \quad w = \begin{cases} m \cdot w, & q \leq 1/m \\ 0, & q > 1/m \end{cases} \quad (17)$$

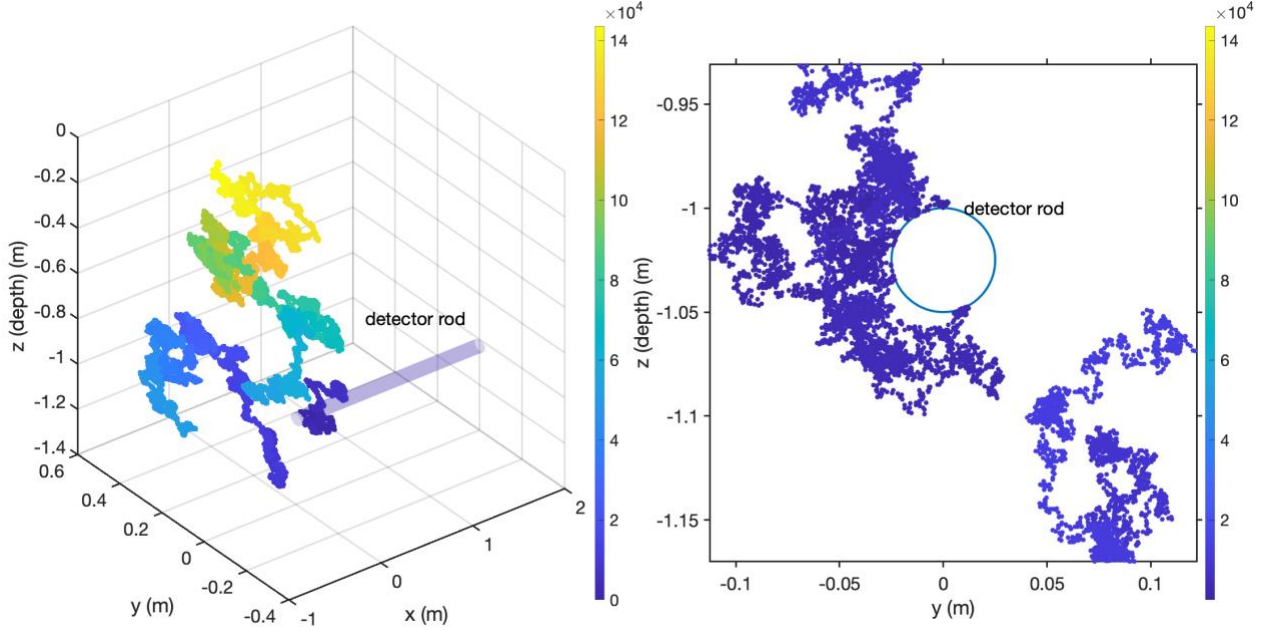
72 where $1/m$ is the probability of photon survival. This technique conserves energy and is unbiased (Wang et al., 1995).
 73 In this study, $w_{\min} = 10^{-5}$ and $m = 10$.

74
 75 At each interaction, the absorbed fraction $\bar{\omega} \cdot w$ is scored into an absorption array in a cylindrical coordinate system
 76 that is used to compute observable quantities of absorption and photon fluence. If a photon packet exits the medium,
 77 it is scored into a transmittance or reflectance array in an azimuthally independent spherical coordinate system that is
 78 used to compute observable quantities of irradiance, radiant intensity, and power. These scoring systems follow the
 79 definitions in Wang et al. (1995) Eq. 4.1–4.32.

80
 81 The preceding sections describe photon transport length, scattering anisotropy, and survival probability. Similar
 82 probability density functions that describe the detector rod interference are described next.

83 **S1.2 Monte Carlo experiment**

84 The detector rod interference is estimated with a “backward” Monte Carlo (BMC) simulation, which simulates photon
 85 trajectories starting from the detector backward to the target (Leathers et al., 2004; Light et al., 2003). Here, the target
 86 is the ice surface. The simulation domain is a 3-dimensional ice slab with one boundary, the ice surface, and otherwise
 87 infinite horizontal and vertical extent. A cylinder with dimensions identical to the detector rod is placed at positions
 88 identical to the measurement depths reported in this paper, and photon packets are released from the irradiance sensor
 89 (“remote cosine receptor”) located on the detector rod (Fig. 1).



90
91
92
93
94
95
96
97
98

Fig. 1: Example Monte Carlo photon tracking simulation from model output used in this study, with interference by cylindrical detector rod. (a) ~14,000 random photon interactions are traced within a 3-dimensional ice volume. The cylindrical object represents the detector rod, here inserted at 1 m below the ice surface. The photon packet is released from the position of the irradiance sensor (“remote cosine receptor”) located on the rod and traced backward to the ice surface (“backward Monte Carlo”). (b) Magnified view of the detector rod in the y-z plane shows photon packets scattering off of the rod. The color-bar represents the number of cumulative interactions experienced by this photon packet.

99 As described above, each interaction within the ice volume is defined by absorption and scattering of the photon by
100 ice. Absorption reduces the photon energy density by an amount $1 - \bar{\omega}_{ice}$. Scattering redirects the photon trajectory
101 according to the Henyey-Greenstein scattering phase function with asymmetry parameter g and transport distance l .
102 Photon interactions with the detector rod require additional specifications that are described next.

103 S1.2.1 Source function for cosine detector

104 The scattering phase function for an irradiance sensor with a cosine response is:

$$105 \quad \tilde{\beta}(\theta) = \frac{\cos \theta}{\pi}, \quad 0 \leq \theta \leq \frac{\pi}{2} \quad (18)$$

106 with probability density function:

$$107 \quad p(\theta) = 2\pi\tilde{\beta}(\theta) \sin \theta \quad (19)$$

108 and cumulative distribution function:

$$109 \quad P(\theta) = 2 \int_0^\theta \cos \theta' \sin \theta' d\theta' = q. \quad (20)$$

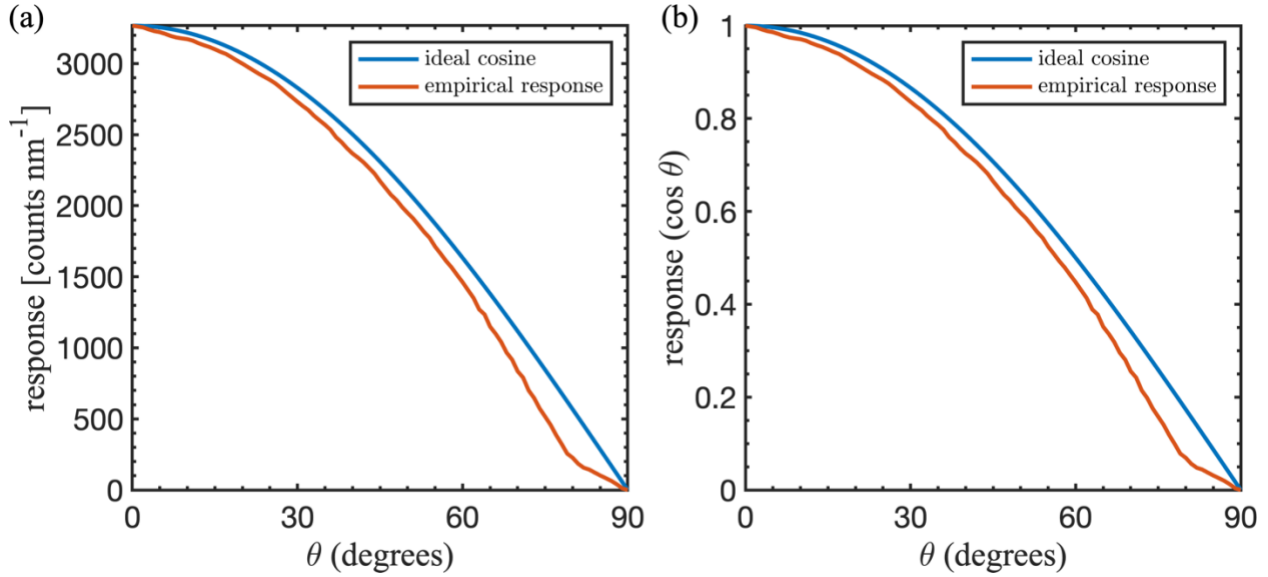
110 Substituting $\mu = \cos(\theta)$ the scattering angle is:

$$111 \quad \cos \theta = \sqrt{1 - q}. \quad (21)$$

112 For a forward Monte Carlo simulation, Eq. 21 gives the probability of photon receipt by an irradiance sensor with an
 113 ideal cosine response. For a BMC simulation, the initial launch trajectory of photons from the irradiance sensor surface
 114 is:

$$\cos \theta = -\sqrt{q}. \quad (22)$$

116 In reality, irradiance sensors do not have an ideal cosine response to radiance. In this experiment, the non-ideal cosine
 117 response of the irradiance sensor is estimated by replacing Eq. 22 with uniform sampling from an empirical probability
 118 density function derived from laboratory measurements of the cosine receptor angular response function provided by
 119 Ocean Optics (Fig. 2). The source azimuth angle ϕ is determined with Eq. (14).



120
 121 **Fig. 2: (a) Comparison of ideal angular response function (ideal cosine) with the empirical angular response function used**
 122 **to estimate the non-ideal response of the irradiance sensor used in this study. The empirical angular response function**
 123 **was developed by Ocean Optics from laboratory measurements on the same irradiance sensor type used in this study. (b)**
 124 **Same as (a) but normalized. The red line in (b) is the empirical probability density function used as the irradiance source**
 125 **function for our backward-Monte Carlo simulations (see Eq. 21–22).**

126 S1.2.2 Scattering and absorption by detector rod

127 If a photon trajectory crosses the 3-dimensional position of the detector rod, the photon energy density is reduced by
 128 an amount $1 - \omega_{\text{rod}}$ and the photon is scattered away from the rod (Fig. 1) with an isotropic scattering phase function:

$$\theta_s = 1 - 2q, \quad (23)$$

$$\phi_s = 2\pi q. \quad (24)$$

131 The collision point is determined with ray tracing formulas that equate the vector equation of the photon trajectory
 132 with the parametric equation for the cylindrical detector rod surface following Ertürk and Howell (2017) Sect. 7.1 Eq.
 133 59–66.

134
 135 The polyvinyl chloride (PVC) detector rod albedo ω_{rod} is estimated from values for the complex refractive index of
 136 PVC (Zhang et al., 2020). Let $\mu = \cos \theta$ be the cosine zenith angle of incident radiation with $\mu = +1$ vertically

137 downward. Following Modest (2013) Section 2.5 Eq. 2.89–2.98, the Fresnel reflectivity and transmissivity to incident
 138 (downward) radiation are:

$$139 \quad R_F(\mu) = \frac{1}{2} \left[\left(\frac{\mu - n\mu_n}{\mu + n\mu_n} \right)^2 + \left(\frac{n\mu - \mu_n}{n\mu + \mu_n} \right)^2 \right] \quad (25)$$

$$140 \quad T_F(\mu) = 1 - R_F(\mu) \quad (26)$$

141 where $n + ik$ and $n_0 + ik_0$ are the complex refractive indices of PVC and air, respectively, and:

$$142 \quad \mu_n = \sqrt{1 - (1 - \mu^2)/n^2} \quad (27)$$

143 is the refracted cosine zenith angle in the PVC pipe. Radiation transmitted into the PVC is attenuated exponentially:

$$144 \quad a(\mu_n) = e^{-\tau/\mu_n} \quad (28)$$

145 where:

$$146 \quad \tau = 4\pi kL/\lambda \quad (29)$$

147 is the optical thickness of the PVC pipe with wall thickness $L = 0.004$ m. Radiation that transmits through L is
 148 internally reflected upward from the inner wall in the direction μ_n and attenuated exponentially along path length τ .
 149 Radiation that reaches the outer wall at $\mu_n > \mu_c$ is partially transmitted across the outer wall according to $T_F(\mu_n)$ and
 150 partially reflected back into the PVC according to $R_F(\mu_n)$, where μ_c is the critical angle given by Snell's law:

$$151 \quad \mu_c = \sqrt{1 - 1/n^2}. \quad (30)$$

152 Formulas for $T_F(\mu_n)$ and $R_F(\mu_n)$ are similar to Eq. 25 and Eq. 26 with modifications for total internal reflection about
 153 μ_c and are given elsewhere (Briegleb and Light, 2007; Liou, 2002).

154
 155 The total reflectivity is estimated with the successive-order-of-scattering method (van de Hulst, 1980), which accounts
 156 for the multiple internal reflections and absorption within the PVC described by Eq. 25–30. We model the PVC pipe
 157 as a plane, which is justified because the radius of curvature is much larger than all wavelengths of light considered
 158 here. For the geometry and optical properties of the detector rod, the total reflectivity has the closed-form solution:

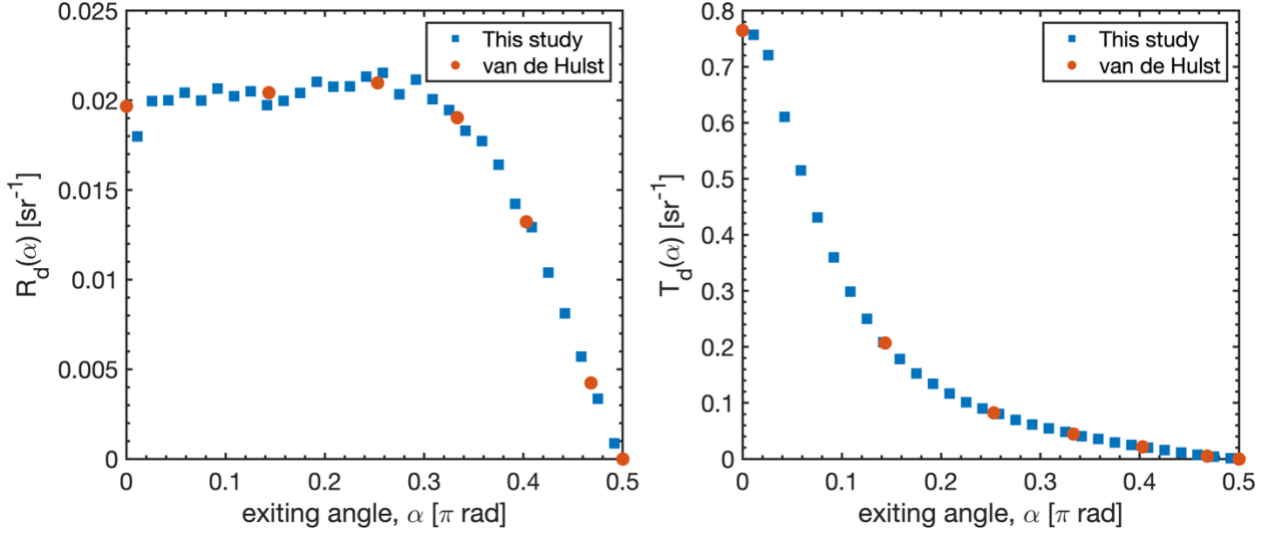
$$159 \quad R_d = R_{F,\mu} + \frac{T_{F,\mu} R_{F,\mu_n} T_{F,\mu_n} a_{\mu_n}^2}{1 - R_{F,\mu_n} a_{\mu_n}^2} \quad (31)$$

160 where the subscripts μ and μ_n on R , T , and a indicate the direction of incident radiance.

161 S2 Model validation

162 The Monte Carlo model described above is verified by comparison with benchmark values for total diffuse reflectance
 163 R_d [W m^{-2}], total transmittance T_t [W m^{-2}], diffuse angular reflectance $R_d(\alpha)$ [W sr^{-1}] and diffuse angular
 164 transmittance $T_d(\alpha)$ [W sr^{-1}] tabulated by van de Hulst (1980). The angular quantities, which have units of radiant
 165 intensity, are defined with respect to the exiting angle normal to the surface α [rad]. For a plane-parallel slab with
 166 optical properties $\sigma_s = 0.9 \text{ m}^{-1}$, $\sigma_a = 0.1 \text{ m}^{-1}$, $g = 0.75$, and optical thickness $\tau = 2$, the van de Hulst (1980) solutions
 167 are $R_d = 0.09739$ and $T_t = 0.66096$. For an ensemble of $N = 100$ simulations, the Monte Carlo model described

168 above gives $R_d = 0.09740 \pm 0.00034$ and $T_t = 0.66098 \pm 0.00049$ ($\mu \pm 1\sigma$). The model closely reproduces the
 169 benchmark solutions for $R_d(\alpha)$ and $T_d(\alpha)$ (Fig. 3).



170
 171 **Fig. 3: Values of diffuse angular reflectance, $R_d(\alpha)$ and transmittance, $T_d(\alpha)$ vs. the photon exiting angle α with respect**
 172 **to the surface normal (after Wang et al. 1995 Fig. 3). Solid circles are benchmark solutions from Table 35 in van de Hulst**
 173 **(1980), which were calculated with the doubling method of solution to the radiative transfer equation.**

174 **S3 Monte Carlo uncertainty estimate**

175 The Monte Carlo model is used to estimate the effect of detector interference on our irradiance measurements and, in
 176 turn, the asymptotic flux attenuation coefficients k_{att} that are estimated from them. To this end, we designed four
 177 experiments that isolate two forms of detector interference: 1) the non-ideal cosine response of the irradiance detector,
 178 and 2) absorption and scattering by the PVC detector rod. The four experiments, including a base simulation with no
 179 detector interference, are summarized in Table S1.

180 **Table S1: Summary of four Monte Carlo experiments that simulate the effect of the detector rod interference on in-ice**
 181 **irradiance measurements. The baseline simulation (ideal diffusion, no rod) has no detector interference.**

Experiment	Source function θ_s	Source function ϕ_s	Detector absorption	Detector scattering
Ideal Diffusion, No Rod	Eq. 23	Eq. 24	-	-
Ideal Cosine, No Rod	Eq. 22	Eq. 24	-	-
Ideal Cosine, With Rod	Eq. 22	Eq. 24	ω_{rod}	Eq. 23-24
Non-ideal Cosine, With Rod	Empirical (Fig. 2)	Eq. 24	ω_{rod}	Eq. 23-24

182
 183 For each experimental setup, the Monte Carlo is integrated across 10,000 interactions at four wavelengths (400 nm,
 184 500 nm, 600 nm, and 700 nm) with detector rod positions that are identical to the measurement depths reported in this
 185 paper (c.f. Fig. 1). For the 20 July experiment, these depths are 9.4 cm, 30.0 cm, 50.5 cm, and 68.6 cm, in units of
 186 solid-ice equivalent (i.e., physical thickness scaled by measured ice density). For the 21 July experiment, these depths

187 are 45.9 cm, 59.0 cm, 73.4 cm, and 114.5 cm. Monte Carlo k_{att} values are estimated for each wavelength with the
188 same method used for the field-estimates, i.e., by linear regression:

189
$$-\log T(z, \lambda) = T_0 + k_{\text{att}}(\lambda)\Delta z + \varepsilon \quad (32)$$

190 where T is the total diffuse transmittance from Monte Carlo simulation (see Section S2), T_0 is a parameter (y-intercept)
191 that represents $T(z = 0)$ and ε is an error term.

192 **References**

- 193 Briegleb, B. P. and Light, B.: A Delta-Eddington Multiple Scattering Parameterization for Solar Radiation in the Sea
194 Ice Component of the Community Climate System Model, Technical Note, National Center for Atmospheric
195 Research, Boulder, Colorado. [online] Available from: <http://dx.doi.org/10.5065/D6B27S71> (Accessed 18 February
196 2019), 2007.
- 197 Ertürk, H. and Howell, J. R.: Monte Carlo Methods for Radiative Transfer, in Handbook of Thermal Science and
198 Engineering, edited by F. A. Kulacki, pp. 1–43, Springer International Publishing, Cham., 2017.
- 199 Gordon, H. R.: Ship perturbation of irradiance measurements at sea 1: Monte Carlo simulations, *Appl. Opt.*, 24(23),
200 4172, doi:10.1364/AO.24.004172, 1985.
- 201 van de Hulst, H. C.: Multiple light scattering: tables, formulas, and applications, Academic Press, New York., 1980.
- 202 Leathers, R. A., Downes, T. V., Davis, C. O. and Mobley, C. D.: Monte Carlo Radiative Transfer Simulations for
203 Ocean Optics: A Practical Guide, Memorandum, Naval Research Laboratory, Washington, D.C. [online] Available
204 from: https://www.oceanopticsbook.info/packages/iws_12h/conversion/files/Leathersetal_NRL2004.pdf (Accessed
205 11 October 2020), 2004.
- 206 Light, B., Maykut, G. A. and Grenfell, T. C.: A two-dimensional Monte Carlo model of radiative transfer in sea ice,
207 *J. Geophys. Res. Oceans*, 108(C7), 3219, doi:10.1029/2002JC001513, 2003.
- 208 Liou, K.-N.: An introduction to atmospheric radiation, 2nd ed., Academic Press, Amsterdam ; Boston., 2002.
- 209 Modest, M. F.: Radiative heat transfer, Third Edition., Academic Press, New York., 2013.
- 210 Mullen, P. C. and Warren, S. G.: Theory of the optical properties of lake ice, *J. Geophys. Res. Atmospheres*, 93(D7),
211 8403–8414, doi:10.1029/JD093iD07p08403, 1988.
- 212 Wang, L., Jacques, S. L. and Zheng, L.: MCML—Monte Carlo modeling of light transport in multi-layered tissues,
213 *Comput. Methods Programs Biomed.*, 47(2), 131–146, doi:10.1016/0169-2607(95)01640-F, 1995.
- 214 Zhang, X., Qiu, J., Li, X., Zhao, J. and Liu, L.: Complex refractive indices measurements of polymers in visible and
215 near-infrared bands, *Appl. Opt.*, 59(8), 2337, doi:10.1364/AO.383831, 2020.

216